AIAA JOURNAL
Vol. 39, No. 6, June 2001

# Jet-Spike Bifurcation in High-Speed Flows

J. S. Shang,* J. Hayes,† K. Wurtzler,‡ and W. Strang†
*U.S. Air Force Research Laboratory, Wright–Patterson Air Force Base, Ohio 45433-7913*

**In recent plasma injection experiments, counterflow jet interaction has been identified as one of the mechanisms that significantly reduces the drag. There is a sudden change of the dynamic state from an oscillatory to nearly steady motion of this jet-shock interaction which depends on the relative magnitude of injection and the stagnation pressure. The shock-wave bifurcation associated with a counterflow jet from a hemispherical cylinder is investigated by a side-by-side experimental and computational effort. Shock-wave bifurcation has been discovered by the present experiments over the entire range of tested conditions in the Mach 6 wind tunnel. This oscillatory motion is sustained by the upstream propagation of selectively amplified frequencies from the free-shear layer to the Mach disk through the embedded subsonic domain. The breakdown of this feedback loop occurs when a higher injecting jet pressure creates a supersonic zone separating the interconnecting embedded subsonic domains.**

## Nomenclature

$D$ = total drag
$p$ = air pressure
$Q$ = conservative variables
$q$ = primitive variable
$r$ = radius of hemispheric nose
$T$ = air temperature
$\bar{u}$ = velocity vector, $u$, $v$, $w$
$\Delta$ = standoff distance of bow shock
$\rho$ = air density

## I. Introduction

IMPROVING aerodynamic performance of aerospace vehicles through drag reduction has been pursued since the days of the Wright brothers. Large drag reduction via plasma or high-temperature gas injection from the stagnation region of a forebody are reported on in recent experiments using a weakly ionized gas.[1–3] An unspecified focused energy deposition upstream of a vehicle has also been analyzed for improving aerodynamic performance.[4] A common feature of these reports is the interaction of the oncoming stream with the introduced flowfield perturbation. As a consequence of the flowfield adjustment to either the counterflow jet or a locally released thermal energy source, favorable flow control can be realized. These particular flow control mechanisms are completely independent of electromagnetic forces.[5,6]

Preliminary research was conducted using unheated air as the injectant to determine the drag reduction by the counterflow jet interaction from electromagnetic forces and nonequilibrium thermodynamics.[7] The total drag of a hemispherical cylinder with and without mass injection was measured by a set of load cells. For the conditions tested, the drag was reduced as much as 30% from the case without mass injection. In addition, the flowfield was found to be unsteady even at the lowest injection rate until the stagnation pressure of the injected air was approached and exceeded a critical point. Beyond the critical value of injection pressure, both the drag force and shock-wave structure settle to a nearly steady state. In essence, a jet-spike bifurcation was observed by this experiment.

The wave drag reduction in aerodynamic applications by either a spike or a jet spike on a blunt-nosed body is well known.[8–12] The wave drag reduction is derived from both the splitting of a single strong shock into multiple shock waves and effectively replacing the blunt body by a slender displacement. Even if the accumulative pressure rise across the multiple and sequential shock waves is identical to that of a single shock, the entropy jump across the multiple wave system is much less. This difference is because the entropy increment across each shock wave is proportional to the cubic power of the pressure jump. The blunt body with injection will, thus, produce a lower wave drag. There are also disadvantages of these drag reduction devices in that they can induce unsteady motion with large-amplitude oscillations through free-shear-layer instability.[7,11]

The unsteady flowfields of spike and jet spike associated with a blunt body were noted a long time ago.[8–10] These self-sustained oscillations have been observed for a wide variety of shear-layer impingement phenomena.[13,14] The highly organized oscillatory fluid motions are sustained by the feedback of upstream pressure propagation through the subsonic recirculating flow region and by a selective amplification of fluctuations in the shear layer. The spike-tipped buzz phenomenon exhibits aerodynamic bifurcation when the length of the spike is extended or retracted from the blunt body to a critical value.[11,15–17] An identical aerodynamic bifurcation for the jet spike is also detected.

For jet-spike interaction, a counterflow jet issues from the foremost point of the blunt body. The supersonic jet expands into a very low stagnation pressure bow shock envelope, then decelerates to a stagnation region, and is terminated by a Mach disk. Then the counterflow jet reverses its orientation as a free shear layer. A part of the jet stream is entrained to form a recirculating region beneath the free shear layer. This complex interacting flowfield constitutes a new displacement shape to the blunt body. As the free shear layer reattaches to the blunt body, the flow realigns with the body contour and also induces a series of compression waves coalescing into a reattachment ring shock. Because the flow displacement is supported by a subsonic recirculating flow and free shear layer, unsteady flow structure is anticipated. The sudden change of dynamic states of the counterflow jet interaction is uniquely governed by the feedback mechanism of the free shear layer and the Mach disk. The selectively amplified frequency leading to resonance is closely tied to the frequency content of the free shear layer, the physical dimensions of the recirculating region beneath the shear layer, and the local acoustic speed. When the selective amplification process and feedback loop can not be maintained, large-amplitude oscillation will cease, and the flowfield tends to return to a nearly steady state. The observed flow phenomenon is complex and requires interpretation of data derived from two different approaches: experimental and computational.

The present effort consists of a side-by-side experimental and numerical study of shock bifurcation over a hemispherical cylinder with mass injection at a freestream Mach number of 5.8. The experimental measurements include schlieren photographs, axial aerodynamic force component measurements, and the spectral data

Received 13 July 2000; revision received 25 October 2000; accepted for publication 25 October 2000. This material is declared a work of the U.S. Government and is not subject to copyright protection in the United States.

*Senior Scientist, Center of Excellence for Computing Simulation. Fellow AIAA.
†Aerospace Engineer, Center of Excellence for Computing Simulation.
‡Aerospace Engineer, Center of Excellence for Computing Simulation. Member AIAA.

of aerodynamic load sensors under the tested conditions. The numerical simulations are generated by solving the three-dimensional, compressible Navier–Stokes equations based on the unstructured grid approach. The calculations are concentrated in the stagnation region, and both laminar flow and turbulent solutions are generated. The detailed flow structure within the displaced shock layer will be delineated by comparing the numerical results with experimental observations.

## II. Experimental Measurements

The test facility for the present effort is a high-Reynolds-number, blow-down wind tunnel designed to simulate flow conditions at a nominal Mach number of 6.0, at the stagnation temperature of 610 K (1100°R), and a range of stagnation pressures from $0.35 \times 10^3$ to $1.4 \times 10^4$ kPa (50 to 2000 psi). The open jet is issued from the nozzle exit with a diameter of 254 mm. The simulated free-stream pressure, therefore, has a range from 2 to 77 torr (0.25 to 10.0 kPa). For the present investigation, the mass flow rate at the stagnation pressure tested ($0.35 \times 10^3$ kPa) is 0.77 kg/s (1.7 lbm/s). This facility can sustain a testing period more than 10 min.

The key parameters for describing counterflow jet phenomenon are the exit conditions of the jet, particularly the exit jet Mach number and the thermodynamic properties of the injectant.[10] Barber introduced the relative mass flow rate as another parameter for counterflow jet experiments.[10] This dimensionless parameter is defined as the jet flow rate per unit area over that of the wind tunnel. He has also demonstrated that when the relative mass flow is less than 3, the shock standoff distances show little or no change. In the present investigation, the maximum mass injection rate of the jet was 0.195 kg/s (4.3 lbm/s), and the experimental data were collected for a parametric range from 6.61 to 423.5.

The most effective way to reduce drag using a jet spike is to achieve the maximum jet penetration and to create both a slender displacement shape and multiple enveloping shock waves in the supersonic oncoming stream. The jet exiting Mach number is a critically important parameter, shown in Fig. 1. The jet spike is generated from a hemispherical cylinder with a nose radius of 38.1 and a length of 292.1 mm (1.5 and 11.5 in.), respectively. Both jets shown are initiated from the identical stagnation pressure and temperature $1.03 \times 10^3$ kPa and 294 K (150 psi and 530°R), respectively. Thus, these jets have the same mass flow, 0.097 kg/s (0.21 lbm/s) but at different jet exit Mach numbers. The basic features of the sonic and supersonic counterflow jets are similar. Both jets are terminated by a Mach disk in the bow shock layer. Then the stagnated jet stream reverses its direction to appear as a free shear layer. The jet–shock interaction significantly modifies the bow shock wave envelope. The free shear layer reattaches upstream to the shoulder of the hemispherical cylinder. The reattachment process in turns creates a stream realignment with the blunt nose and induces a ring shock. The main difference in the flowfield structure between the sonic and supersonic jet is that the jet with an exiting Mach number of 2.84 increased the standoff distance to twice the sonic injection value.

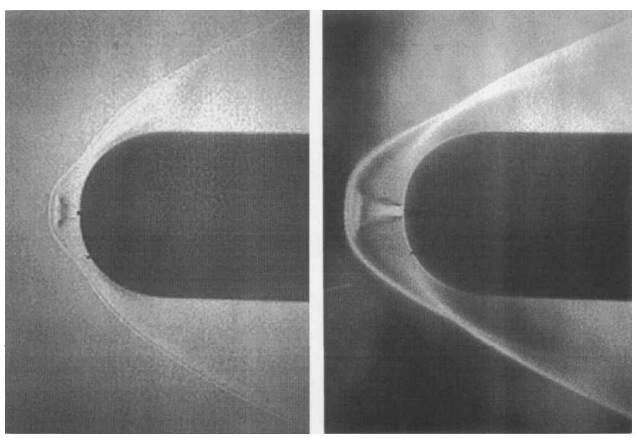

**Fig. 1 Effect of jet exit Mach number on flow structure.**

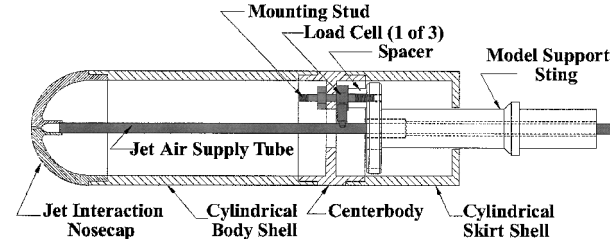


**Fig. 2 Force measuring model.**

Nevertheless, no attempt was placed on the present effort to optimize the jet spike ahead of the blunt body to achieve the maximum wave drag reduction. Instead, the tested model is designed to generate an exiting Mach number of 2.84 by a slender conical nozzle with a sonic throat diameter of 2.44 mm (0.096 in.) and an exit diameter of 4.65 mm (0.183 in.) at a distance of 12.7 mm (0.5 in.) downstream. With the fixed nozzle geometry at a constant stagnation temperature condition, the only control parameter of the jet spike is either the stagnation pressure of the jet or the jet mass flow rate. Similarly, the simulations at different altitudes are controlled by the tunnel operational stagnation pressure at a minimum stagnation temperature of 610 K for condensation free flow. Therefore, all of the drag measurements are collected at a combination of tunnel and jet stagnation pressures.

Because jet spike bifurcation and drag reduction are the primary interest, the data collection is focused on the force measurement, spectral data of oscillating motion, and schlieren photographs. The drag data are recorded by a set of three load cells and prestressed by a force of 2.2 kN (495 lbf) to operate in the linear measuring range. The test model is isolated from the support strut by these load cells to receive the total axial aerodynamic force exerted on the model. The force measuring model is shown in Fig. 2. In this arrangement, the wave drag, skin-friction drag, and the base pressure drag are not separable but measured together. The spectral information of the oscillating force data is recorded by a dynamic signal analyzer, Hewlett–Packard Model 3562, with a frequency range up to 100 kHz.

## III. Numerical Analysis

An experimental and computational side-by-side investigation is essential for studying the complex self-sustained fluid motion highlighted by a jet-spike shock bifurcation. The detailed dynamic event of the counterflow jet and its associated multiple shock-wave structure can only be obtained by solving the time-dependent, three-dimensional Navier–Stokes equations. The system of governing equations is solved by an implicit, unstructured Euler/Navier–Stokes solver, Cobalt.[18,19] The basic algorithm is based on the Godunov's Riemann formulation and implicit time stepping to yield second-order spatial and temporal accuracy.[20,21] The numerical procedure is developed for a cell-centered, finite volume approach and is able to accommodate a single grid system that may consist of a variety of cell types, tetrahedron and hexahedron, in three-dimensional space. The neighbor-cell connectivity of a unstructured gird formulation also enhances an exceptionally scalable, parallel computing performance when this numerical procedure is ported to multicomputers using a message passing interface library.[22]

The governing differential equations are discretized by the fully implicit numerical scheme and can be recast as

$$[3(\boldsymbol{Q}^{n+1} - \boldsymbol{Q}^{n}) - (\boldsymbol{Q}^{n} - \boldsymbol{Q}^{n-1})]/2\Delta t + \nabla \cdot \boldsymbol{F} = 0 \qquad (1)$$

where the $\boldsymbol{Q}$ are independent vectors of conserved variables, $\boldsymbol{Q} = (\rho, \rho u, \rho v, \rho w, p)$ and $\boldsymbol{F}$ are the flux vectors of the Navier–Stokes equations. The details of this formulation may be found in Ref. 18. However, several interesting features of the Cobalt code need to be mentioned.

First, the reconstruction of flux vectors at the centroid of the cell faces is based on the estimated primitive variable, $q(\rho, u, v, w, p)$ by a least-squares solution to the following approximation:

$$q_{i \pm \frac{1}{2}} = q_i \pm \vec{r} \cdot \nabla q_i \qquad (2)$$

where $q^{\pm}_{i\pm 1/2}$ are the reconstructed left- and right-side primitive variables at the centroid of the cell face for the Riemann problem and $\nabla q_i$ is the gradient vector for cell $i$.

The three-dimensional formulation includes all of the nearest neighbor cells and the solution to the gradient vector yields a matrix relation, $\bar{\bar{A}} \cdot q_i = (q_m - q_i)$. For Cobalt, the overdetermined matrix $\bar{\bar{A}}$ is solved by a QR factorization,[23] $\bar{\bar{A}}$ is factored into an orthogonal matrix Q times an upper-triangular R, to attain a greater stability over that of a lower–upper (LU) decomposition for the high aspect ratio cell structure. The gradient calculation then requires only a matrix–vector multiplication:

$$\nabla q_i = \Sigma^m \omega_i^m (q_m - q_i) \tag{3}$$

where $\omega_i^m = (R^{-1}\boldsymbol{Q}^t)_i^m$ is the least-squares weight vector of cell $i$ associated with all nearest-neighbor cells in the QR factorization of $\bar{\bar{A}}$.

Another unique feature of Cobalt rests on the computation of viscous fluxes. In fact, the calculation process must possess three basic attributes: It satisfies the conservation law, the discrete maximum principle, and $\nabla \cdot \nabla q = 0$ for a linear field. In Cobalt, the gradient flux vector is split to include a normal and tangential component $\nabla q^m = (\nabla q^m)_n + (\nabla q^m)_t$. The tangential gradient flux vector is taken as the average of the two cells adjacent to the interface. Meanwhile, the tangential component is also used to evaluate the normal component:

$$(\nabla q^m)_n = \frac{\left[q_m - (\nabla q^m)_t \cdot \overline{\boldsymbol{r}_i^m}\right]}{\left|\bar{n} \cdot \overline{\boldsymbol{r}_i^m}\right|} \tag{4}$$

where $\overline{\boldsymbol{r}_i^m}$ is the unit vector connecting the adjacent centroid of a given cell $i$. The components of gradient construction in this manner ensures the linearity-preserving property for $q$ in a linear field. The ultimate goal is to achieve, a conservative, positive, and linearity-preserving scheme.

These unique features plus an ingenious limiter have enhanced the cell-center, finite volume, unstructured grid procedure to control effectively the numerical dissipation and simultaneously to maintain the robustness for solving problems even with poor grid topologies.

In the present application, the no-slip velocity components and adiabatic temperature conditions are imposed on the blunt-body surface. For the far field, the unperturbed freestream condition at the upstream and the no-reflection condition downstream are specified. The turbulent closure is achieved by the Spalart–Allmaras one-equation model.[24]

The computational error is assessed by generating three consecutive solutions on increasingly refined grids. For the shock-dominant problem, the error criterion for evaluation is the shock definition and the standoff distance. The flowfield around the hemispherical cylinder at a freestream Mach number of 5.8 and Reynolds number based on nose diameter of $3.458 \times 10^5$ is calculated on three different grid systems that consist of 185,484, 256,824, and 303,804 cells. In Fig. 3, the Mach number distributions along the stagnation streamline of these calculations are presented. The calculated shock standoff distances, defined by the sonic point of the captured shock, essentially are grid independent after the first grid refinement. The calculated and measured standoff distances compare very well with the correlated data of Ambrosio and Wortman.[25] The normalized values by the nose radius are $\Delta / r = 0.155$, 153, and 0.157, respectively. The Mach number distributions from the second and the final mesh refinement are limited to a maximum discrepancy of less than 3.4%. For the finest mesh system, the average law-of-the-wall variable $y^+$ is less than unity. The finest grid distribution is adopted for the rest of the present computations.

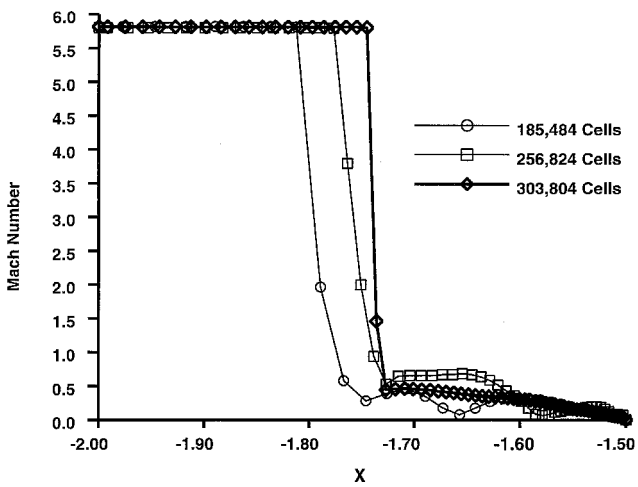


**Fig. 3 Effect of grid resolution on standoff distances.**

Based on the aforementioned criterion and the focused interest on shock-wave structure, the difference in jet interaction between the laminar and turbulent computation is important. For the laminar computation, the very short jet penetration into the shock layer and multiple separated flow topology that surrounds the counterflow jet are not supported by the experimental observation. Therefore, only the numerical results with a turbulent closure are included in the following discussion.

## IV. Experimental Findings

The shock bifurcation of a jet spike is shown in Fig. 4. Six schlieren photographs are included at a tunnel stagnation condition of $T_0 = 610$ K (1100°R) and $p_0 = 6.89 \times 10^2$ kPa (100 psi). Each photograph represents the six different jet stagnation pressures normalized by a fixed tunnel stagnation condition, $p_j / p_0$. The flowfield becomes unsteady even at the lowest injection pressure level of 0.148. As the jet stagnation pressure increases, the length of jet penetration upstream increases accordingly. Because of the unsteady aerodynamic motion, the image of the jet-induced shock wave in the schlieren photograph becomes blurred by multiple exposures. Meanwhile, the amplitude of oscillatory motion is also increased until it reaches a maximum around $p_j / p_0 = 0.90$. At this point, a bifurcation of shock wave structure takes place, and further increases in jet stagnation pressure do not alter this complex shock structure significantly. The magnitude of oscillation also decreases to near the level of flow without jet injection. Similar shock bifurcations were also observed for all of the other wind-tunnel stagnation pressure settings.

The spectral data of the oscillatory drag force sensor under the tested conditions are presented in Fig. 5. For the present investigation, the range of the spectral signal was found to be less than 500 Hz. Only two typical data sets are included in the presentation, one of them describes the oscillatory motion when the jet spike is

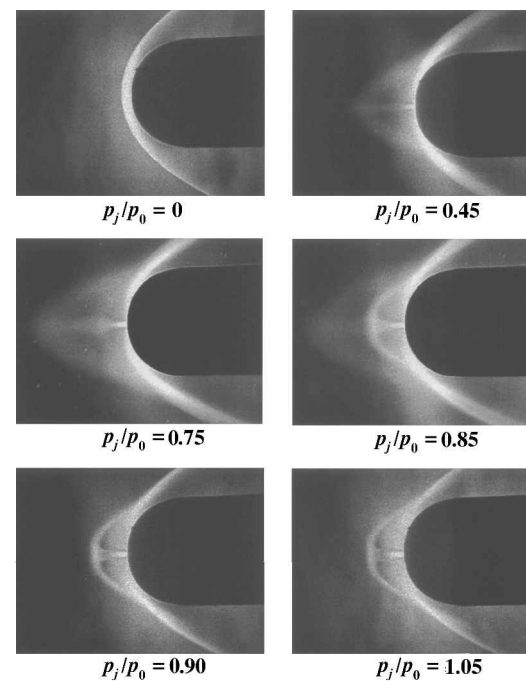


**Fig. 4 Jet-spike shock bifurcation.**

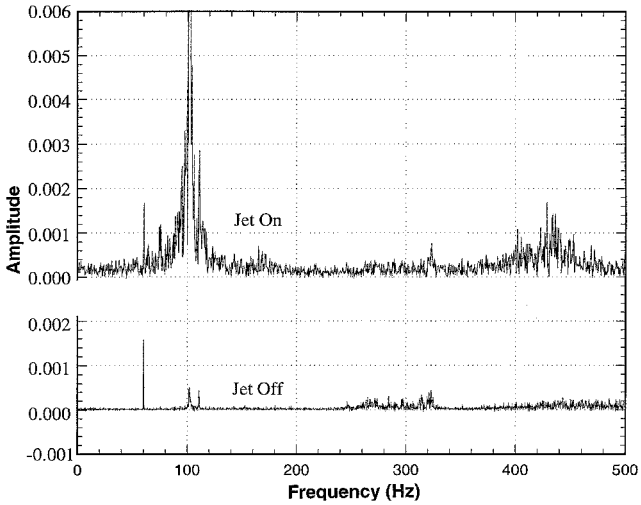


Fig. 5 Spectra data of drag force.

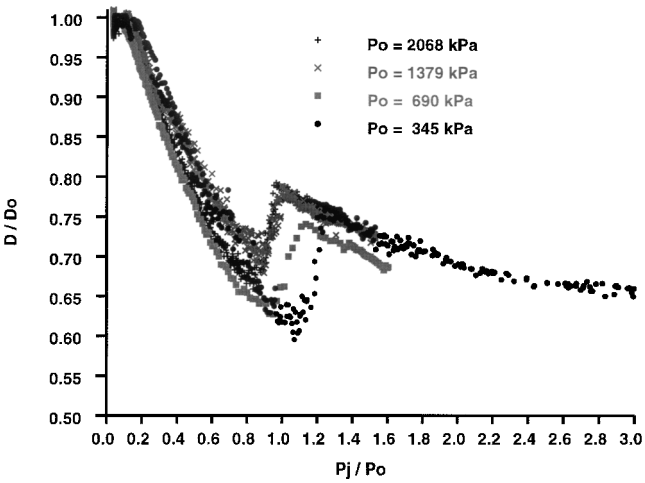


Fig. 6 Drag measurements of jet-spike bifurcation.

near the bifurcation. At this critical point of the dynamic event, at least two dominant frequencies around 100 and 440 Hz are easily detected. The standard deviation of drag measurement at this critical state grows rapidly by a factor of 11.72 relative to the no-injection condition. The standard deviation of fluctuating drag measurements also reaffirms the observation that the jet-spike induced unsteadiness diminishes after the injection pressure exceeds a critical value at the bifurcation point.

In Fig. 6, the measured drag force normalized with respect to the no-injection case at different jet and wind-tunnel stagnation conditions are given. The flowfields are generated at four wind tunnel stagnation pressures, $p_0 = 0.345 \times 10^3$, $0.689 \times 10^3$, $1.379 \times 10^3$, and $2.068 \times 10^3$ kPa (50, 100, 200, and 300 psi), all at a stagnation temperature of $T_0 = 610$ K. The measured data represent the total axial force exerted on the entire model, including the wave drag, skin-friction drag, base drag, and the reverse thrust of the counterflow jet. In general, the critical points of bifurcation described by the stagnation pressure ratio of jet and tunnel, $(p_j)_0/p_0$, are bracketed in the range from 0.8 to 1.05. The value of the critical point increases as the tunnel stagnation pressure decreases.

The overall behavior of the drag force variation with counterflow jets at four different wind-tunnel stagnation pressures is similar. The measured drag is lower than the baseline, or the no-injection case, even at the lowest jet injection pressure. The drag reduction due to shock shape modification overwhelms completely the reverse thrust by the counterflow jet. Although there are variations among the drag force distributions at difference wind-tunnel conditions, the drag reduction is as low as 60% of the baseline case at the shock bifurcation point. At the highest tunnel pressure tested, the drag reduction by the counterflow jet is still more than 30%. The shock bifurcation generally occurs at a higher jet injection pressure for higher wind-tunnel stagnation pressures. This behavior is easily understood by recognizing that the counterflow jet has to encounter a higher exiting pressure within the shock layer. As will be shown in the following discussion, the cutoff of the feedback loop by a local supersonic region requires a higher jet stagnation pressure.

Beyond the bifurcating point, the measured drag force first rises sharply and then sustains a continuous drop with a shallow slope. All test results exhibit identical behavior. In short, the counterflow jets have continuously expanded into the lower exit pressure in the shock layer of the tested pressure range. At the lowest tunnel stagnation pressure, decreasing drag persists up to the highest counterflow pressure tested, $(p_j)_0/p_0 \leq 2.85$.

In Fig. 7, the measuring process is examined to assess the data scattering band at the lowest tunnel pressure $p_0 = 0.345 \times 10^3$ kPa (50 psi). Two procedures for data recording were used. The majority of data was collected by sweeping the load cell output at a scan rate of 0.25 s. In this data recording mode, 1000 data points were obtained in 20 s after the model injected into the test chamber and a steady flowfield was detected. Another test procedure measured a single point at one run. A total of five points at different counterflow stagnation pressures was recorded in this manner. From these measurement procedures, the data scatter is determined to be around 6.5%.

## V. Numerical Results Validation

To understand better the observed shock bifurcation, the results of numerical and experimental simulation must be analyzed together. The side-by-side effort focuses on the validation of the computed results on both global behavior and detailed flowfield structure. The comparison of measured and calculated drag force normalized by the baseline case is presented in Fig. 8. These data are for the wind-tunnel stagnation pressure of $0.689 \times 10^3$ kPa (100 psi). The

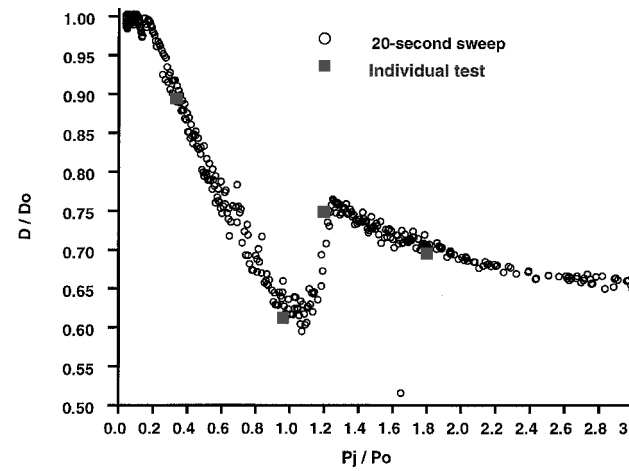


Fig. 7 Verification of drag measurement procedures.

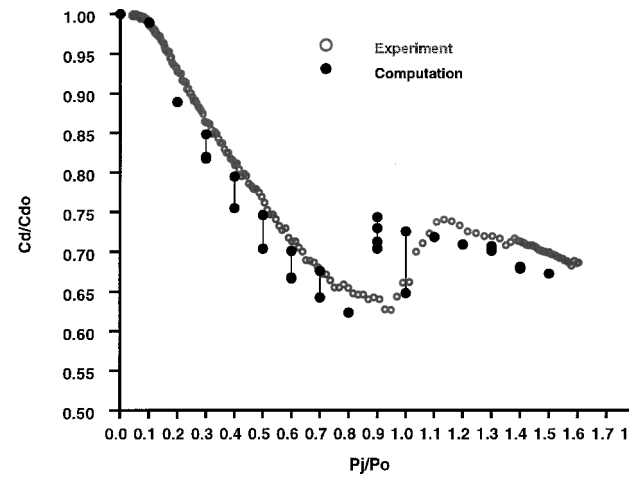


Fig. 8 Drag computation of jet-spike bifurcation.

calculated drag force using the mass-averaged Navier–Stokes equations with a turbulent closure[24] includes the base drag correction from experimental measurements. The base drag evaluated from two pressure taps in the model base region yields a nearly constant value of 2.558 N (0.575 lbf) over the entire injecting pressure range. However, the aerodynamic interference by the stem support is unaccountable. Therefore, the comparison with data is meaningful as long as the wave drag is the dominant force of the flowfield. In addition, because the flowfield is unsteady, the calculated results will depict an oscillating range instead of an ensemble value from experiments. In spite of the aforementioned constraints, reasonable agreement is noted over a large range of the injection pressure tested including the bifurcation.

The comparison of the observed and computed shock structures across the critical point of bifurcation can be more definitive than the integrated drag force. The shock-wave structures at the values of $p_j/p_0 = 0.75$ and 1.05, at the wind-tunnel stagnation pressure of $0.689 \times 10^3$ kPa (100 psi), are selected for presentation. Figure 9 shows the shock-wave structure before the critical point of bifurcation, $p_j/p_0 = 0.75$. Because the Mach disk responds to the unsteady shear layer surrounding the counterflow jet, the complex shock envelope is highly unsteady and appears as a blurred image in the schlieren photograph. On the other hand, the computed schlieren image is sampled at a given instant in time and, thus, yields a clearly defined flowfield structure. The counterflow jet and the ring shock induced by the reattached free shear layer are clearly identified. The computed result exhibits good agreement with experimental observation. The overall dimension of the computed shock structure, particularly the standoff distance at the time of sampling, represents the lower limit ($\Delta/r = 1.21$) within the experimental observed band ($1.21 \leq \Delta/r \leq 1.77$).

In Fig. 10, the shock structure for $p_j/p_0 = 1.05$ is given. At this injection pressure, the shock-wave structure has jumped to a nearly steady state. The schlieren photograph yields a sharper image than the highly unsteady motion in the lower injection pressure range. Under this condition, the Mach disk, which terminates the forward motion of the jet, and the coalesced reattaching waves to form the ring shock are clearly exhibited. Even the slip stream originating from the intersection of the bow shock and ring shock is clearly visible. For the nearly steady flowfield, both the measured and computed standoff distance shows an identical value of $\Delta/r = 0.74$. The agreement of the overall flowfield structure between the measured and the computed result is excellent.

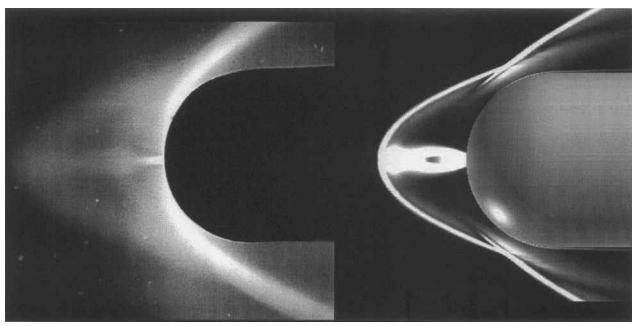

**Fig. 9 Comparison of computed schlieren and photograph; $p_j/p_0$ = 0.75.**

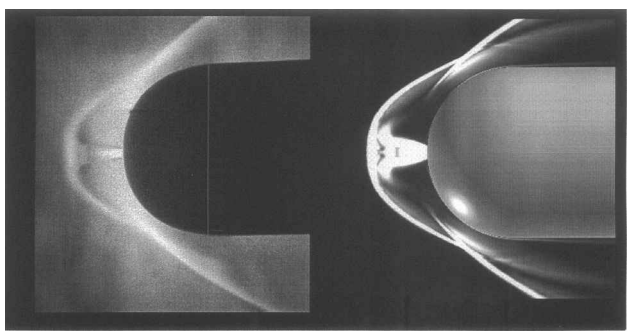

**Fig. 10 Comparison of computed schlieren and photograph; $p_j/p_0$ = 1.05.**

## VI. Discussion of Results

The detailed flowfield structure of the counterflow jet can be easily delineated by the validated numerical results. To put the steady and unsteady flowfield structure on an equal footing, the particle traces in the plane of symmetry at a given instance are shown in Fig. 11. The oscillatory flow for the lower injection case, $p_j/p_0 = 0.75$, is on the left-hand side of Fig. 11. The higher injection case, $p_j/p_0 = 1.05$, for which the flowfield has jumped across the critical point of bifurcation into the nearly steady-state condition, is on the right-hand side of Fig. 11. The predominant flowfield structure is similar in that the underexpanded, counterflow jet interacting with the oncoming stream through the bow shock creates a recirculated flow region. This recirculation zone is three dimensional and resembles the open crater of a volcano or geyser. The forward motion of the counterflow jet ceases immediately downstream of a Mach disk, reverses its direction, and becomes a free shear layer over the recirculating zone. The free sheer layer eventually reattaches to the hemispherical cylinder. The reattachment process triggers a series of compression waves that coalesce into a ring shock.

The free shear layer and the recirculation zone possess multiple inflection points in velocity and mass flow ($\rho\vec{u}$) profile, which is inherently unstable with a rich content of frequency spectrum. Meanwhile, the upstream pressure propagation is made possible by the mostly subsonic recirculating region to close a feedback loop through the local stagnation region downstream of the Mach disk. The closed feedback loop is essential to amplify selectively small perturbations to achieve a self-sustained oscillation. Therefore, the frequency spectrum of this oscillatory motion is determined by the characteristics of the free shear layer, the length dimension of the subsonic conduit, and the local speed of sound. However, the resonating oscillatory motion of the flowfield, including the shock waves, will cease if the feedback loop is interrupted.

In Fig. 12, the Mach number contours of the two cases across the critical point of the bifurcation are given. Again, a snapshot of the unsteady motion is on the left-hand side, and the steady motion after the jump is on the right-hand side of Fig. 12. For the lower injection rate case, the recirculating zone beneath the free shear layer and the subsonic region immediately downstream of the Mach disk are completely embedded in the supersonic flowfield. The feedback loop

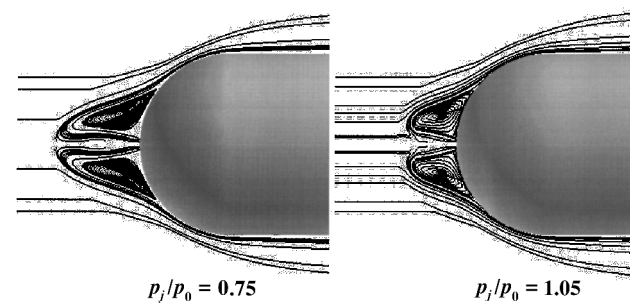


**Fig. 11 Particle trace of jet spike in plane of symmetry.**

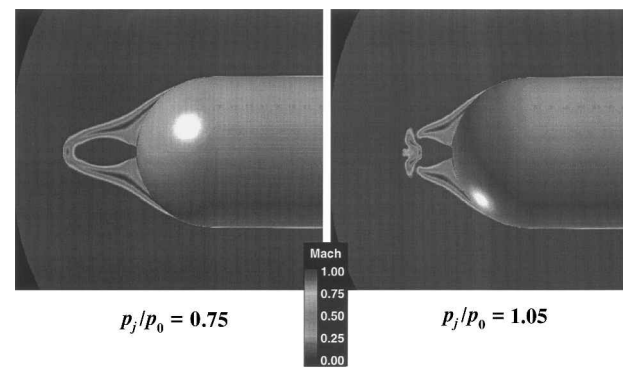


**Fig. 12 Mach number contours of jet spike.**

from the unstable free shear layer to the Mach disk is, therefore, closed. Any perturbation generated by the free shear layer must propagate through the embedded subsonic domain to influence the Mach disk formation. Any amplifiable frequency of the free-shear-layer stability through the feedback loop is capable of achieving a resonance. For the present investigation, two dominant and discrete frequencies have been identified at 100 and 440 Hz.

After an injection pressure exceeds the critical point of the bifurcation as shown in the right-hand side of Fig. 12, the supersonic jet stream now separates the recirculating zone beneath the free shear layer and the subsonic region immediately downstream of the Mach disk. Separation of the disturbance generating source and the amplifier effectively cut off the feedback mechanism. The oscillatory flow motion ceases, or at least is substantially subdued. This observation is confirmed by both experiment and computation.

The drag reduction by the counterflow jet can be explained in part by the multiple shock-wave structure that reduced the entropy production significantly in contrast to a single enveloping bow shock wave. The jet spike also creates a new displaced shape that is more efficient in reducing the wave drag than the blunt body. The displaced shapes of the jet spike are shown in Fig. 13. In fact, the maximum drag reduction is achieved consistently at the critical point of the bifurcation. At this condition, the counterflow jet attains the maximum penetration into the shock layer to produce the most slender displacement configuration. However, the flowfield is unsteady with a large magnitude aerodynamic fluctuation.

The calculated pressure distribution on the hemispherical cylinder in terms of the pressure coefficient $C_p$ is presented in Fig. 14. Again the $C_p$ distributions were calculated for the tunnel stagnation pressure of $0.689 \times 10^3$ kPa (100 psi). Because there are no available data for the purpose of validation, the $C_p$ distributions are given in consecutive discretized nodes on the body surface. It is clearly exhibited that the surface pressure reaches the second peak at the free shear reattachment. The local maximum is decreasing with the increasing injection pressure. The lower attachment pressure level

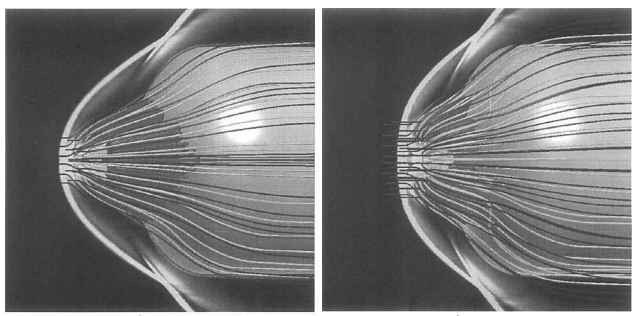


**Fig. 13 Displacement shape defined by jet interaction.**

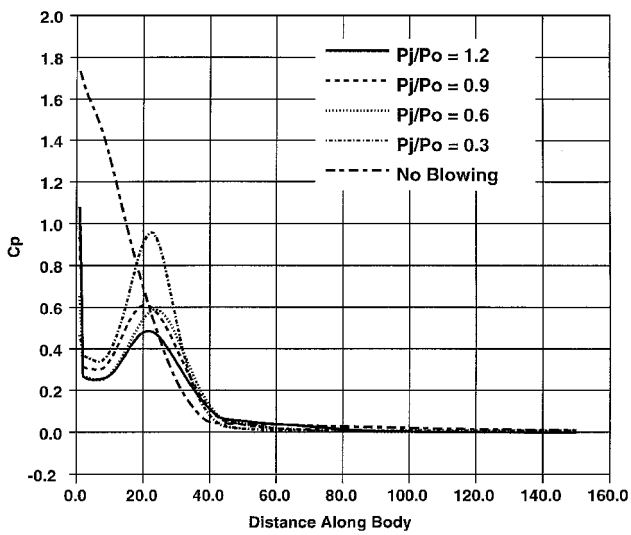


**Fig. 14 Pressure distribution on the body surface.**

reflects a decreasing total drag measurement, as observed in the experiments.

## VII. Conclusions

A shock bifurcation of the counterflow jet and shock-wave interaction has been discovered by the presented experiment. This phenomenon defined the dynamic range of a feedback resonance between the free-shear-layer instability and the Mach disk of this flowfield.

The jet-spike bifurcation experiment reveals a critical state for oscillatory fluid motion. The control parameter is the stagnation pressure ratio between the oncoming stream and the counterflow jet. At lower injection pressures, a self-sustained oscillatory motion is maintained by a feedback loop between the free shear layer over the recirculating zone surrounding the jet spike and the Mach disk. When the counterflow jet is generated by a sufficiently high stagnation pressure, a supersonic stream separates the embedded subsonic domain to break down the feedback loop, resonance ceases, and returns to a steady motion.

The critical point of bifurcations can be quantified by the stagnation pressure ratio between tunnel and the counterflow jet. For the cases tested, the critical point varies from a value of 0.80 at higher tunnel stagnation pressures to a value of 1.05 at the lowest tunnel stagnation pressure tested.

The drag reduction for the hemispherical cylinder at a Mach number of 5.8, using a cold counterflow jet, will reach a minimum at the bifurcation then rise sharply. The maximum drag reduction near the bifurcation has an oscillatory value as high as 40%. However, for the tested conditions, the drag reduction varies from 30 to 40%, depending on the operating stagnation pressure. The drag force after an initial rise at the critical point continuously decreases with increasing injection pressure under the present conditions. The present finding suggests a rigorous reexamination of drag reduction procedures using plasma injection techniques.

## Acknowledgments

The research team deeply appreciates the sponsorship by Steven Walker of the Air Force Office of Scientific Research. The invaluable contributions by Robert Peterkin Jr. and the wind-tunnel crew, Hank Baust, Joe Martin, Tom Norris, Ray Raber, Glenn Williams, Sam Prather, and Michael Greene, are duly acknowledged. The computing resource was supported in part by a grant from the Department of Defense High Performance Computing Shared Resource Centers at Wright–Patterson Air Force Base.

## References

[1]Ganiev, Y. C., Gordeev, V. P., Krasilnikov, A. V., Lagutin, V. I., Otmennikov, V. N., and Panasenko, "Theoretical and Experimental Study of the Possibility of Reducing Aerodynamic Drag by Employing Plasma Injection," AIAA Paper 99-0603, Jan. 1999.

[2]Bityurin, V. A., Velikodny, V. Y., Klimov, A. I., Leonov, S. B., and Potebnya, V. G., "Interaction of Shock Waves with a Pulse Electrical Discharge," AIAA Paper 99-3533, June–July 1999.

[3]Malmuth, N. D., Fomin, V. M., Maslov, A. A., Fomichev, V. P., Shashkin, A. P., Korotaeva, T. A., Shipyuk, A. N., and Pozdnyakov, G. A., "Influence of a Counterflow Plasma Jet on Supersonic Blunt Body Pressures," AIAA Paper 99-4883, Nov. 1999.

[4]Riggins, D. W., Nelson, H. F., and Johnson, E., "'Blunt-Body Wave Drag Reduction Using Focused Energy Deposition," *AIAA Journal*, Vol. 37, No. 4, 1999, pp. 460–467.

[5]Shang, J. S., "An Outlook of CEM Multidisciplinary Applications," AIAA Paper 99-0336, Jan. 1999.

[6]Shang, J. S., Canupp, P. W., and Gaitonde, D. V., "Computational Magneto-Aerodynamic Hypersonics," AIAA Paper 99-4903, Nov. 1999.

[7]Shang, J. S., Ganguly, B., Umstattd, R., Hayes, J., Arman, M., and Bletzinger, P., "Developing a Facility for Magneto-Aerodynamic Experiments," AIAA Paper 2000-0447, Jan. 2000.

[8]Finley, P. J., "The Flow of a Jet From a Body Opposing a Supersonic Free Stream," *Journal of Fluid Mechanics*, Vol. 26, Pt. 2, 1966, pp. 337–368.

[9]Bogdonoff, S. M., and Vas, I. E., "Preliminary Investigations of Spiked Bodies at Hypersonic Speeds," *Journal of the Aerospace Sciences*, Vol. 26, No. 1, 1959, pp. 65–74.

[10]Barber, E. A., Jr., "An Experimental Investigation of Stagnation-Point Injection," *Journal of Spacecraft and Rockets*, Vol. 2, No. 5, 1965, pp. 770–774.

[11]Shang, J. S., Hankey, W. L., and Smith, R. E., "Flow Oscillations of Spike-Tipped Bodies," *AIAA Journal*, Vol. 20, No. 1, 1982, pp. 25, 26.

[12]Calarese, W., Shang, J. S., and Hankey, W. L., "Investigation of Self-Sustained Shock Oscillations on a Spike-Tipped Body at Mach 3," *Proceedings of ASME Winter Annual Meeting*, American Society of Mechanical Engineers, Fairfield, NJ, 1981, pp. 151–156.

[13]Rockwell, D., and Naudascher, E., "Self-Sustained Oscillations of Impinging Free Shear Layers," *Annual Review of Fluid Mechanics*, Vol. 11, 1979, pp. 67–94.

[14]Shang, J. S., and Hankey, W. L., "Numerical Simulation of Self-Excited Oscillations in Fluid Flows," *Recent Advances in Numerical Methods in Fluid*, edited by W. G. Habashi, Vol. 3, Pineridge, Swansea, England, U.K., 1984, pp. 543–582.

[15]Harney, D. J., "Oscillating Shocks on Spiked Nose Tips at Mach 3," U.S. Air Force Flight Dynamics Lab., Rept. AFFDL-TM-79-9-FX, Wright–Patterson AFB, OH, 1979.

[16]Reding, J. P., "Fluctuating Pressures on Mildly Indented Nosetips," *Journal of Spacecraft and Rockets*, Vol. 16, No. 5, 1979, pp. 302–310.

[17]Demetriades, A., and Hopkins, A. T., "Asymmetric Shock-Wave Oscillations on Spiked Bodies of Revolution," *Journal of Spacecraft and Rockets*, Vol. 13, No. 11, 1976, pp. 703, 704.

[18]Strang, W. Z., Tomaro, R. F., and Grismer, M. J., "The Defining Methods of $Cobalt_{60}$: A Parallel, Implicit, Unstructured Euler/Navier–Stokes Flow Solver," AIAA Paper 99-0786, Jan. 1999.

[19]Tomaro, R. F., Witzeman, F. C., and Strang, W. Z., "A Solution on the F-18C for Store Separation Simulation Using $Cobalt_{60}$," AIAA Paper 99-0122, Jan. 1999.

[20]Godunov, S. K., "A Difference Scheme for Numerical Computation of Discontinuous Solution of Hydrodynamic Equations," *Sbornik Mathematics*, Vol. 17, 1959, pp. 271–306.

[21]Tomaro, R. F., Strang, W. Z., and Sankar, L. N., "An Implicit Algorithm for Solving Time-Dependent Flows on Unstructured Grids," AIAA Paper 97-0333, Jan. 1997.

[22]Grismer, M. J., Strang, W. Z., Tomaro, R. F., and Witzeman, F. C., "Cobalt: A Parallel, Implicit, Unstructured Euler/Navier–Stokes Solver," *Advances in Engineering Software*, Vol. 29, April–July 1998, pp. 365–373.

[23]Golub, G. H., and Van Loan, C. F., *Matrix Computations*, 2nd ed. Johns Hopkins Press, Baltimore, MD, 1989, pp. 211–259.

[24]Spalart, P. R., and Allmaras, S. R., "A One-Equation Turbulence Model for Aerodynamic Flows," AIAA Paper 92-0439, Jan. 1992.

[25]Ambrosio, A., and Wortman, A., "Stagnation Point Shock Detachment Distance for Flow Around Spheres and Cylinder," *ARS Journal*, Vol. 32, No. 2, 1962, p. 281.

P. Givi
*Associate Editor*